Title

A mesoscale model for interface-mediated plasticity: Investigation of ductile and brittle fracture

Journal

Mechanics of Materials, 221

ISSN

0167-6636

Authors

Yu, Jinxin
Ngan, Alfonso HW
Srolovitz, David J
et al.

Publication Date

2026-10-01

DOI

10.1016/j.mechmat.2026.105798

Mechanics of Materials 221 (2026) 105798

Contents lists available at ScienceDirect

Mechanics of Materials

journal homepage: www.elsevier.com/locate/mecmat

Research paper

A mesoscale model for interface-mediated plasticity: Investigation of ductile and brittle fracture

Jinxin Yu [a,c], Alfonso H.W. Ngan [b,d], David J. Srolovitz [b,*], Jian Han [a,*]

[a] Department of Materials Science and Engineering, City University of Hong Kong, Hong Kong Special Administrative Region of China
[b] Department of Mechanical Engineering, The University of Hong Kong, Pokfulam Road, Hong Kong Special Administrative Region of China
[c] Department of Materials Science and Engineering, University of California, Los Angeles, CA, United States
[d] School of Metallurgy and Materials, University of Birmingham, Edgbaston, Birmingham B15 2TT, United Kingdom

ARTICLE INFO

Invited Editor Jean-F Molinari

Keywords:
Interface/Grain boundary
Fracture
Mesoscale model

ABSTRACT

The presence of grain boundaries significantly impacts the mechanical properties of crystalline materials, particularly when dealing with micro- or nano-scale samples. The nature of dislocation-grain boundary interactions governs the macroscopic plastic behavior. We employ a mesoscale interface boundary condition, incorporating with a two-dimensional continuum dislocation dynamics framework, to investigate these dislocation-grain boundary interactions, examining both single- and multiple-slip numerical cases. The simulations show that, apart from affecting strength and ductility, the accumulation of dislocations near a grain boundary generates stress concentrators and initiates intergranular brittle fracture. Consequently, dislocation-grain boundary interactions manifest a competition between ductile and brittle failure modes upon loading. We further analyze the upturn in strain hardening rate across a range of interfacial reaction kinetics, which can be attributed to the competition between the rates of dislocation accumulation and interfacial reactions at the grain boundary.

1. Introduction

Most natural crystalline materials and those of technological interest are polycrystalline, i.e., composed of single crystal grains of different crystallographic orientations separated/delimited by grain boundaries (GBs). The mechanical properties of polycrystals, including their mechanical strength, ductility, and fracture behavior, are strongly influenced by the properties and spatial arrangement of these GBs (in addition to the intrinsic properties of the crystals) (e.g., see Kheradmand et al. (2010), Zhu and Wu (2023)). In metallic systems, the well-known and widely applicable Hall-Petch relation posits that reducing the mean grain size leads to increased strength (even approaching the theoretical strength) (Hall, 1951; Javaid et al., 2021). However, there is also a well-known trade-off with ductility; reducing grain size usually results in decreased ductility (Meyers et al., 2006; Ovid'Ko et al., 2018; Wang et al., 2023). In recent years, heterostructured materials have shown promise in achieving improved combinations of strength and ductility, attributed to hetero-deformation induced (HDI) strengthening (Ji et al., 2023; Zhu et al., 2021). This suggests that designing appropriate interfaces and/or optimizing their spatial distribution may provide a viable route to overcome this strength-ductility trade-off. In particular, the key feature is the nature of the interactions between dislocations and interfaces. Extensive *in situ* experiments have revealed that the interactions between lattice dislocations and interfaces are complex and go beyond simple dislocation blocking (Kacher and Robertson, 2012; Kacher et al., 2014; Kacher and Robertson, 2014). Since dislocations are the carriers of plastic deformation, these interactions directly affect the plastic deformation of materials, subsequently impacting their strength and ductility.

When a dislocation approaches a grain boundary (GB), it may be transmitted into the adjacent grain, absorbed by the GB, reflected back, or blocked. The dislocation-GB interaction can be thus represented as a Burgers-vector reaction involving the lattice dislocations in the two grains and the carriers of plastic shear within the GB. If the GB is a coherent or semi-coherent interface, these carriers are well-defined GB dislocations. If the GB is general in the sense that its structure is highly disordered, plastic shear is accommodated by shear bands, like those observed in the deformation of amorphous materials. Unlike dislocations, the shear magnitude carried by a shear band is continuous, rather than quantized; thus, its effective "Burgers vector" (or disregistry) can be considered arbitrary. Therefore, for all GB types, dislocation-GB interactions can be consistently modeled as Burgers-vector reactions.

In our recent work (Yu et al., 2025), we proposed a mesoscale *interface boundary condition* (BC) to describe the Burgers-vector reactions at interfaces of crystalline materials. In this framework, the reaction

* Corresponding authors.
E-mail addresses: srol@hku.hk (D.J. Srolovitz), jianhan@cityu.edu.hk (J. Han).

https://doi.org/10.1016/j.mechmat.2026.105798
Received 18 January 2026; Received in revised form 6 June 2026; Accepted 2 July 2026
Available online 9 July 2026

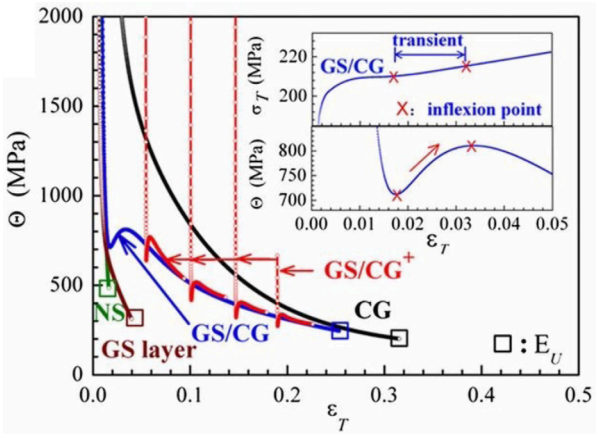

Fig. 1. Typical experimental results for strain hardening rate (Θ) versus true strain (ε_T), reproduced with permission from Wu et al. (2014) (Copyright 2014 PNAS). Curves correspond to: coarse-grained (CG) sample (black), nanostructured (NS) film (green), grain-size gradient structured (GS) layer (dark red), gradient structured and coarse-grained (GS/CG) sandwich sample (blue), and the same sandwich sample subjected to unloading–reloading tensile tests (red). (For interpretation of the references to color in this figure legend, the reader is referred to the web version of this article.)

constant serves as a measure of the rate at which Burgers-vector reactions occur at the interface. Notably, the reaction constant depends on the detailed bicrystallography and atomic structure of the interface/GB. This (atomic-structure-informed) reaction rate determines the rate of dislocation transmission/reflection, thereby exerting a strong influence on the overall plastic deformation of materials. In the limiting case where the reaction constant is effectively zero (i.e., the interface is impenetrable), dislocation motion is confined to within a grain. Such a case is often assumed in mesoscale simulations (Jiang et al., 2019), leading to the predicted flow stresses significantly higher than experimental measurements. Typically, interfacial reactions relax these flow stresses. For example, interactions between lattice dislocations and coherent twin boundaries can be accommodated by the propagation of twinning partials as well as dislocation transmission, resulting in enhanced strength without compromising ductility (Lu et al., 2004; Li et al., 2010). Given that the Burgers-vector reaction constant is intrinsically determined by GB structure, GB engineering may modify the mechanical response of polycrystals.

Another intriguing phenomenon in polycrystals is how GBs and their distribution influence the strain hardening rate; in particular, how the strain hardening rate varies with strain. The strain hardening rate, defined as $\Theta \equiv \partial\sigma/\partial\varepsilon$, i.e., the slope of the stress–strain curve, quantifies the work hardening behavior, which is closely associated with ductile fracture following necking. In tensile experiments, the strain hardening rate commonly monotonically decreases with increasing true strain. However, for heterostructured materials, a transient strain hardening regime typically appears at low tensile strains, as exemplified by the blue curve in Fig. 1 for the gradient-structured/coarse-grained (GS/CG) sandwich steel samples (Wu et al., 2014, 2015). This regime exhibits an upturn in the strain hardening rate Θ with increasing true strain. Unloading–reloading curves for the same material further reveal a similar upturn in Θ upon each reloading cycle; see the red curves in Fig. 1. Notably, the GS/CG sandwich sample exhibits a slower decay in Θ compared to the gradient-structured (GS) sample, although not compared to the coarse-grained (CG) sample, as shown in Fig. 1. This behavior indicates enhanced strain hardening retention in the GS/CG sample relative to the GS sample, leading to better ductility. By contrast, both the standalone GS layer and CG samples display a conventional, monotonic decrease in Θ (see the GS layer and CG curves in Fig. 1), suggesting that the observed Θ upturn arises only from the heterostructure. One possible explanation for this Θ upturn is scarcity of mobile dislocations at the onset of plastic deformation (Wu et al., 2015). Another explanation attributes the Θ upturn to the high back stress resulting from the strain incompatibility caused by microstructural heterogeneity (Yang et al., 2021). Although these qualitative explanations of the experimental observations provide some insights, a more clear and predictive model for this behavior remains elusive. We re-examine these observations using our mesoscale interface reaction model here to provide more quantitative insights into these phenomena.

This paper employs numerical simulations to investigate how interfaces affect plasticity in polycrystalline materials. The main challenge lies in properly incorporating the microscopic mechanisms of dislocation-GB interactions into the simulation framework. To address this, we build a model based on the crystallographically-rigorous interface reaction model developed previously (rather than on widely used phenomenological laws) (Yu et al., 2025, 2024). We then apply this mesoscale interface BC with a well-developed two-dimensional (2D) continuum dislocation dynamics (CDD) model (Leung et al., 2015; Ngan, 2017). The primary focus of this study includes:

(i) The role of GB properties in macroscopic mechanical response of materials. GB properties determine Burgers-vector reaction rates at GBs and interfacial strength. When GB reaction kinetics cannot keep pace with dislocation generation inside grains, GBs provide strengthening and resist necking while promoting dislocation accumulation and the onset of intergranular fracture (Stroh, 1957; Cottrell, 1965).

(ii) The origin of the upturn exhibited in strain hardening curves. This provides a possible mechanism for the experimentally observed upturn in strain hardening rate vs. strain arising from the competition between GB reaction kinetics and the dislocation generation rates inside grains, with the balance tuned by the interface reaction constant.

The remainder of this paper is organized as follows. First, we briefly introduce the CDD model used to describe plasticity within grains and review the mesoscale interface BC. We then present several simulation cases to validate the model. Next, we apply the interface BC to study plastic deformation and mechanical properties for several GBs over a range of interface reaction constants. We analyze the transition from ductile to brittle fracture under varying conditions (strain rates and interface reaction constants). Finally, we examine the strain hardening rate vs. strain for a set of interface reaction constants and dislocation generation rates, to rationalize the upturn associated with GB strengthening.

2. Methodology

2.1. Model, kinematics, and interface boundary condition

Consider a periodic bicrystal model; its geometry is given in Fig. 2. Focus on a GB (labeled by "I") that divides two grains ("α" and "β"). Slip systems in the grains are characterized by slip directions and slip plane normal vectors $(\mathbf{s}^{(i)}, \mathbf{n}^{(i)})$ $((i) = \alpha_1, \alpha_2, \beta_1, \beta_2, \ldots)$. We distinguish dislocations with opposite Burgers vector signs and denote them by "+" and "−". A +/− dislocation on slip system (i) moves in the positive/negative slip direction when the resolved shear stress (RSS) $\tau^{(i)} > 0$, where the sign of $\tau^{(i)}$ determined by the definition of $\mathbf{n}^{(i)}$. Dislocation density $\rho^{(i)}_{+/-}$ is the number of positive/negative dislocations on the slip system (i) per unit area, which evolves following:

$$\dot{\rho}^{(i)}_{+/-} = -\cos\theta^{(i)} \frac{\partial}{\partial x}\left(\rho^{(i)}_{+/-} v^{(i)}_{+/-}\right) - \sin\theta^{(i)} \frac{\partial}{\partial y}\left(\rho^{(i)}_{+/-} v^{(i)}_{+/-}\right) + \dot{\rho}^{(i),\mathrm{ann}}_{+/-} + \dot{\rho}^{(i),\mathrm{gen}}_{+/-}, \tag{1}$$

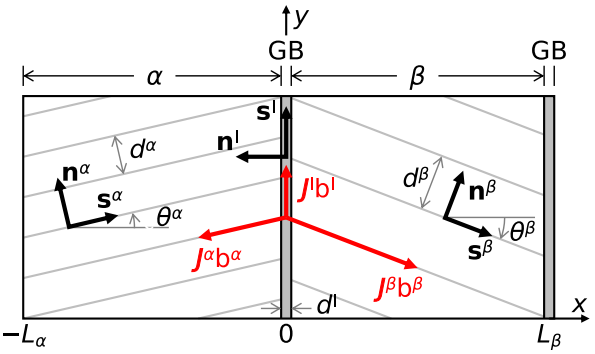

Fig. 2. Configuration of a system composed by α and β grains separated by GBs. Periodic boundary conditions are applied along the x- and y-axes. Gray lines denote slip planes. Black vectors denote slip directions and the normal vectors of slip plane. Red vectors denote Burgers vector fluxes from a point of a GB into α and β grains and along the GB. (For interpretation of the references to color in this figure legend, the reader is referred to the web version of this article.)

which describes conservation of dislocations on each slip system. In Eq. (1), θ is the inclination of slip plane and $v_{+/-}^{(i)}$ is the velocity of positive/negative dislocations on slip plane (i). Dislocation annihilation rate follows: $\dot{\rho}_{+}^{(i),\mathrm{ann}} = \dot{\rho}_{-}^{(i),\mathrm{ann}} = -\rho_{+}^{(i)}\rho_{-}^{(i)} r_{\mathrm{c}} |v_{+}^{(i)} - v_{-}^{(i)}|$, where r_{c} is the capture radius which approximately equals to dislocation core size. Dislocation generation rate follows (Kocks et al., 1975): $\dot{\rho}_{+}^{(i),\mathrm{gen}} = \dot{\rho}_{-}^{(i),\mathrm{gen}} = \eta |\tau^{(i)}|^{p}$, where the parameters p and η are the exponent and dislocation source intensity. The power-law constitutive relation is adopted:

$$v_{+}^{(i)} = -v_{-}^{(i)} = \begin{cases} v_0 \,\mathrm{sgn}(\tau^{(i)}) \left| \frac{\tau^{(i)} - \tau_{\mathrm{f}}}{\tau_0} \right|^{n}, & |\tau^{(i)}| - \tau_{\mathrm{f}} > 0 \\ 0, & |\tau^{(i)}| - \tau_{\mathrm{f}} \le 0, \end{cases} \tag{2}$$

where v_0 and τ_0 are constants, τ_{f} denotes the Peierls stress, i.e., the minimum shear stress required to move a unit-length dislocation, and n is a constant exponent (Yu et al., 2025; Argon, 2007). The factor $\mathrm{sgn}(\tau^{(i)})$ guarantees the correct direction of dislocation motion. Specifically, when $|\tau^{(i)}| > \tau_{\mathrm{f}}$ and $\tau^{(i)} > 0$, a dislocation with a positive Burgers vector moves in the positive slip direction ($v_{+}^{(i)} > 0$), while a dislocation with a negative Burgers vector moves in the opposite direction ($v_{-}^{(i)} < 0$).

Dislocation-GB interactions are treated by a mesoscale interface BC we developed previously (Yu et al., 2025); formulation of the interface BC is restated here only for completeness. Consider a general case where there are N (≥ 4) non-colinear slip systems in the two grains; the GB can also be treated as a slip system. An arbitrary reaction "(k)" may occur among any four of the N slip systems. The kinetics of reaction "(k)" may be described by

$$\mathbf{J}_{(k),\mathrm{I}} = \kappa_{(k)} \mathbf{B}^{-1} (\mathbf{c} \otimes \mathbf{c})_{(k)} \mathbf{B} \mathbf{T}_{(k),\mathrm{I}} \boldsymbol{\rho}_{(k),\mathrm{I}}, \tag{3}$$

where the subscripts "(k)" and "I" represent reaction "(k)" and the GB where all quantities are evaluated, $\kappa_{(k)}$ is the reaction constant for reaction "(k)", $\mathbf{J}_{(k),\mathrm{I}} \equiv \left(J^{(1)}, J^{(2)}, J^{(3)}, J^{(4)}\right)^{\mathrm{T}}$ is a list of dislocation fluxes, $\boldsymbol{\rho}_{(k),\mathrm{I}} \equiv \left(\rho^{(1)}, \rho^{(2)}, \rho^{(3)}, \rho^{(4)}\right)^{\mathrm{T}}$, $\mathbf{c} \equiv \left(c^{(234)}, c^{(314)}, c^{(124)}, c^{(132)}\right)^{\mathrm{T}}$ with $c^{(ijk)} \equiv \mathbf{s}^{(i)} \cdot (\mathbf{s}^{(j)} \times \mathbf{s}^{(k)})$ $(i, j, k = 1, 2, 3, 4)$, $\mathbf{B} \equiv \mathrm{diag}\left(b^{(1)}, b^{(2)}, b^{(3)}, b^{(4)}\right)$ is an array of Burgers vectors, and $\boldsymbol{\tau}_{(k),\mathrm{I}} \equiv \mathrm{diag}\left(\tau^{(1)}, \tau^{(2)}, \tau^{(3)}, \tau^{(4)}\right)$ is an array of resolved shear stresses. The interface reaction constant $\kappa_{(k)}$ depends on the microscopic dislocation-GB reaction mechanisms, GB structure, material properties, and temperature. Based on harmonic transition state theory, $\kappa_{(k)}$ may be expressed as $\kappa_{(k)} = \kappa_0 \exp(-Q_{(k)}/k_{\mathrm{B}}T)$, where $Q_{(k)}$ is the activation barrier for dislocation reactions at the GB (Yu et al., 2025). Different interfaces, such as coherent twin boundaries, low-angle GBs, and general high-angle GBs, are therefore expected to exhibit different $\kappa_{(k)}$ values. In principle, $Q_{(k)}$ may be determined from atomistic simulations or inferred experimentally from activation-volume measurements (Zhu et al., 2007). In the present study, $\kappa_{(k)}$ is varied parametrically to investigate the mesoscale effects of different GB reaction kinetics. Similar relations apply to all combinations of any four slip systems. The total dislocation flux, due to all $M \equiv C_N^4$ reactions, is

$$\bar{\mathbf{J}}_{\mathrm{I}} = \sum_{k=1}^{M} \bar{\mathbf{J}}_{(k),\mathrm{I}} = \bar{\mathbf{B}}^{-1} \left[\sum_{k=1}^{M} \kappa_{(k)} \overline{(\mathbf{c} \otimes \mathbf{c})}_{(k)} \right] \bar{\mathbf{B}} \bar{\mathbf{T}}_{\mathrm{I}} \bar{\boldsymbol{\rho}}_{\mathrm{I}}, \tag{4}$$

where $\bar{\mathbf{B}} \equiv \mathrm{diag}(b^{(1)}, \ldots, b^{(N)})$, $\bar{\mathbf{T}}_{\mathrm{I}} \equiv \mathrm{diag}(\tau^{(1)}, \ldots, \tau^{(N)})$, $\bar{\boldsymbol{\rho}}_{\mathrm{I}} \equiv (\rho^{(1)}, \ldots, \rho^{(N)})^{\mathrm{T}}$, and $\bar{\mathbf{J}}_{\mathrm{I}} \equiv (J^{(1)}, \ldots, J^{(N)})^{\mathrm{T}}$. See our previous work for more details about this interface BC (Yu et al., 2025).

In the simulations below, we adopt dimensionless quantities, defined as:

$$\tilde{\rho} \equiv \rho L_x^2, \quad \tilde{L} \equiv L/L_x, \quad \tilde{t} \equiv v_0 t / L_x, \quad \tilde{v} \equiv v/v_0, \quad \tilde{\tau} \equiv \tau/K, \tag{5}$$

where L denotes any quantity with the dimension of length, L_x is the length of the simulation cell in the x-direction, and $K \equiv G/[2\pi(1-\nu)]$ (with G and ν being the shear modulus and Poisson's ratio, respectively). The reaction constant is defined as ($\kappa = \kappa_0 e^{-Q/k_{\mathrm{B}}T}$), and its dimensionless form is expressed as ($\tilde{\kappa} = \kappa/\kappa_0$). The numerical simulation details and parameters are presented in Appendix A and in Table 1, respectively. It should be noted that in Table 1, the superscript i is omitted because we assume that the parameters are identical for all slip systems (including GB).

Table 1
Dimensionless parameters for the two-dimensional continuous dislocation dynamics simulations. For simplicity, we choose the same parameters for all slip systems of two grains (including the GB).

Parameters	Values (dimensionless)
Burgers vector magnitude, $\tilde{b}$	1×10^{-3}
Annihilation capture radius, $\tilde{r}_{\mathrm{c}}$	1×10^{-3}
Time step, $\Delta\tilde{t}$	3×10^{-5}
Length of unit cell along x axis, $\tilde{L}_x$	1.0
Exponent in the velocity power law, n	1
Slip resistance, $\tilde{\tau}_0$	0.1
Peierls stress, $\tilde{\tau}_{\mathrm{f}}$	1×10^{-2}
Source intensity, $\tilde{\eta}$	1×10^{8}
Source term exponent, p	2

2.2. Validation: Impenetrable interfaces

Consider first the case in which dislocations cannot cross or react with the GB; this corresponds to a Neumann boundary condition (BC) at the interface (i.e., shown as the vertical dashed lines in the periodic simulation cell in Fig. 3(a)). The model has only one grain α with orientation $\theta^{\alpha} = 30°$, i.e., the angle between the slip direction $\mathbf{s}^{\alpha}$ and the x-axis as shown in Fig. 3(a). The dislocation sources are assumed to exist at every (mesh) point in the microstructure; here, we employ a 50×50 mesh. When an external shear stress ($\tilde{\sigma}_{xy}^{\mathrm{ext}} = 0.01$) is applied, the RSS activates the dislocation sources and drives the glide of opposite-signed dislocations in opposite directions. Since there is no dislocation flux crossing the GBs, all dislocations pile up against the GBs, as seen in Fig. 3(a) and (b). Qualitatively, the dislocation density distribution along the x-axis exhibits a sharp increase close to the GBs and decays rapidly with distance from the GBs, as depicted in Fig. 3(b) (Scardia et al., 2014). Fig. 3(c) shows that the total RSS τ, indicated by the dashed blue line, decays to zero over time. As the dislocations pile up at the GB, they induce a back stress that counteracts the external RSS, shutting off the dislocation sources.

From Fig. 3(b) and (c), we observe that the peak dislocation density within the pile-up adjacent to the GB increases with mesh refinement (i.e., as the mesh size decreases). The dislocation density in a mesh element equals to the number of dislocations in this element divided by

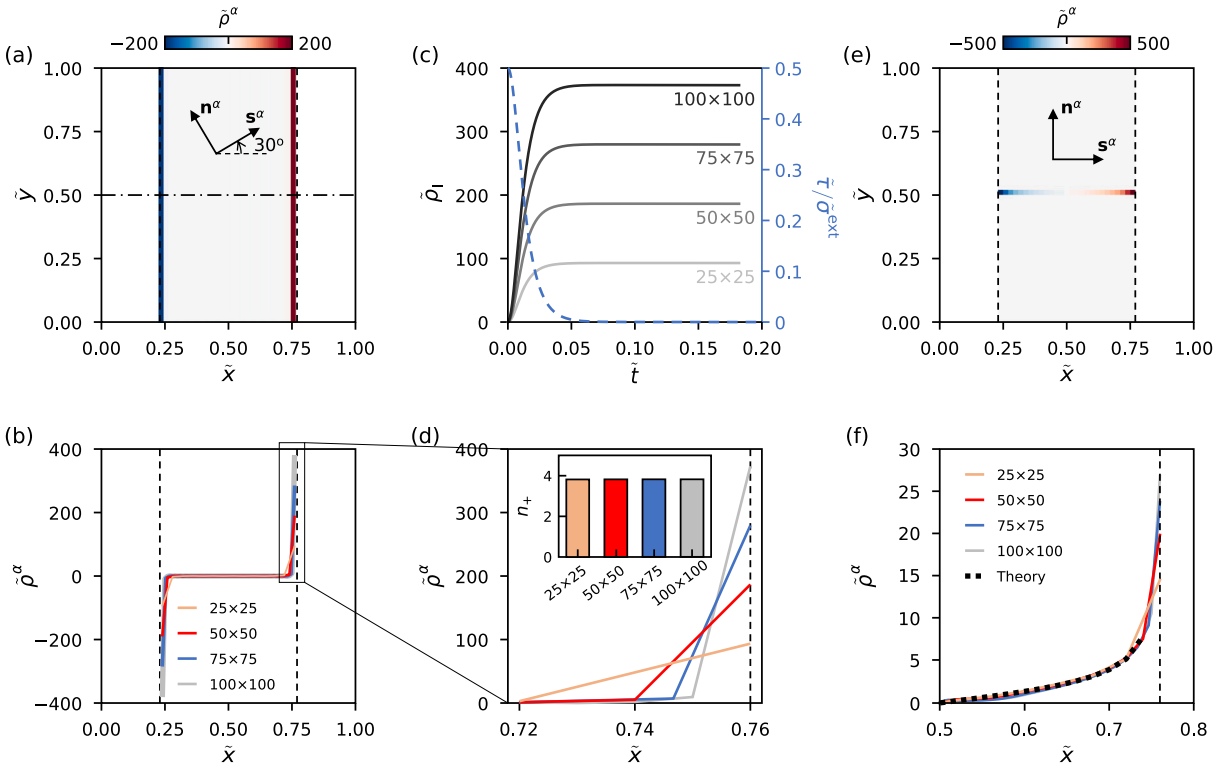

Fig. 3. Simulation results for a periodic bicrystal geometry under an applied shear stress of $\tilde{\sigma}^{\text{ext}}_{xy} = 0.01$. (a) shows the distribution of dislocation density over the whole region ($\theta^{\alpha} = 30°$) at final states for simulations with a 50 × 50 mesh; (b) shows the distribution of dislocation density along the x-direction with different mesh sizes; (c) shows the evolution of dislocation density at the interface $\tilde{\rho}_{\text{I}}$ (i.e., the dislocation density at the GB, $\tilde{x} = 0.76$) and averaged resolved shear stress $\tilde{\tau}$ within the grain for different meshes; (d) enlargement of the dislocation density spatial distribution from (b) near the interface ($\tilde{x} = 0.76$) and the inset shows the magnitude of the dislocation density localized within one mesh point of the interface; (e) the distribution of dislocation density for the case where there is a single dislocation source located at the center of the unit cell (mesh size 50 × 50 and $\theta = 0°$); (f) shows the distribution of dislocation density along x-axis for the case shown in (e) for several mesh sizes.

the mesh size. In the limiting case where all dislocations are concentrated at the GB, i.e., in the element next to the GB, refining the mesh should increase the dislocation density in this element while leaving the number of dislocations unchanged. The total number of positive dislocations is estimated by $n_{+} = \sum_{i,j} \tilde{\rho}^{\alpha}_{+}(i,j)\Delta\tilde{x}\Delta\tilde{y}$, where (i,j) index the mesh elements, and $\Delta\tilde{x}$ and $\Delta\tilde{y}$ denote the mesh sizes in the two directions. We find that n_{+} is independent of the mesh size; see the inset of Fig. 3(d). The mesh-insensitivity of the total number of dislocations demonstrates the robustness of our simulation results.

Now, consider the case where the simulation cell contains only one point source located at the center $(\tilde{x}', \tilde{y}')$. The source term may be described as $\tilde{\rho}^{\text{gen}}_{+} = \tilde{\rho}^{\text{gen}}_{-} = \tilde{\eta}|\tilde{\tau}|^{p}\delta(\tilde{x} - \tilde{x}', \tilde{y} - \tilde{y}')$, where $\delta(\tilde{x} - \tilde{x}', \tilde{y} - \tilde{y}')$ represents the Dirac delta function. The unit cell is also periodic in both the x- and y-directions with Neumann BCs. The slip system in the center crystal is $\theta^{\alpha} = 0°$; all other parameters are the same as shown in Table 1. As shown in Fig. 3(e), positive and negative dislocations glide along the slip plane and pile up against the interface. Since there is only one slip plane in the unit cell, the distance between sources and slip planes along which dislocation glides is large; i.e., set by the periodic unit cell size in the y-direction, $100b$ (where b is the magnitude of Burgers vector). The dislocation density profile obtained from our simulation results can be compared to the theoretical result derived based on a single slip plane (Hirth and Lothe, 1982). As seen in Fig. 3(f), the agreement between the simulation and the theory is excellent. This validates the basic simulation model. A typical simulation using a 100 × 100 mesh requires approximately 4–5 h in the current Python implementation. The present framework is readily extendable to larger 2D polycrystalline systems and, potentially, to 3D simulations, provided that computational efficiency is further optimized.

2.3. Fracture criteria

The material may undergo either ductile or brittle fracture, depending on the loading conditions and intrinsic material properties (Zhu and Li, 2010). We consider ductile failure under tensile loading in terms of the necking criterion proposed by Hart (Hart, 1967). In this framework, strain localization occurs when the work hardening in the material is unable to compensate for the increment of load:

$$\Theta \leq (1 - m)\sigma, \tag{6}$$

where $\sigma(\varepsilon, \dot{\varepsilon})$ is the stress as a function of strain ε and strain rate $\dot{\varepsilon}$, $\Theta \equiv (\partial\sigma/\partial\varepsilon)_{\dot{\varepsilon}}$ is the strain hardening rate, and $m \equiv (\partial \ln\sigma/\partial \ln\dot{\varepsilon})_{\varepsilon}$ is the strain rate sensitivity. While the Hart criterion applies to rate-dependent materials, the Considère condition may be used for rate-independent materials: $\Theta \leq \sigma/(1 + \varepsilon)$, where the stress $\sigma(\varepsilon)$ only depends on strain ε. We focus here on the Hart criterion.

Brittle fracture, on the other hand, is characterized by limited microplasticity, which microcracks nucleating at interfaces and subsequently coalescing to cause sudden fracture. In the dislocation-based theory of brittle fracture introduced by Stroh, fracture occurs when the stress at the tip of a dislocation pile-up at the interface exceeds the stress required for interfacial decohesion (Stroh, 1957; Liu et al., 2023). Although other dislocation-based fracture models have also been proposed (Cottrell, 1965; Smith and Barnby, 1967), they are not directly applicable to the present model because they are formulated for a single slip plane. Our continuum model incorporates an infinite array of possible slip planes; see Fig. 2.

As illustrated in Fig. 4(a) and (b), we consider a microcrack of length $2a$ produced by the pile-up dislocations at the GB, and analyze the crack propagation under the shear and normal stresses: σ^{GB}_{xx}, σ^{GB}_{xy},

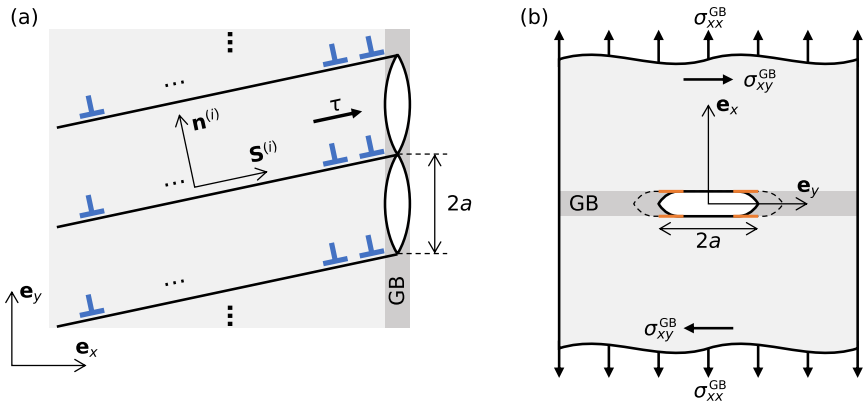

Fig. 4. The fracture nucleation scheme based on the linear elastic fracture model with infinite slip plane along y-direction. (a) There are n piled up dislocations on each slip plane under resolved shear stress τ, leading to microcrack initiation near the interface/GB for two-dimensional model; (b) the stress field induced by piled up dislocation acting at the GB with a microcrack of length $2a$. The orange line segments in (b) show the new surfaces created during crack propagation.

and σ_{yz}^{GB}, associated with the dislocations from within the grains (and the GB disconnections). In the linear elastic theory of fracture, the crack will extend when the energy release rate is sufficient to overcome the change in surface/interface energy, which can be expressed as Weertman (1996)

$$\frac{K_I^2(1-\nu)}{2G}+\frac{K_{II}^2(1-\nu)}{2G}+\frac{K_{III}^2}{2G}=2\gamma_{eff}. \tag{7}$$

where K_I, K_{II}, and K_{III} are the mode I, II, and III stress intensity factors associated with the total stress, respectively, and $\gamma_{eff}=2\gamma-\gamma_I$ represents the effective work for GB decohesion, with γ and γ_I being the fracture surface energy and the GB energy, respectively.

In this study, the mode III stress intensity factor K_{III} is not relevant because of the 2D nature of the model. The stress intensity factors for an assumed slit-like crack of length $2a$ can be determined from the stresses at the GB, σ_{xx}^{GB} and σ_{xy}^{GB}:

$$K_I=\sigma_{xx}^{GB}\sqrt{\pi a},\quad K_{II}=\sigma_{xy}^{GB}\sqrt{\pi a},\quad K_{III}=0, \tag{8}$$

where the superscript "GB" indicates the stresses evaluated at the GB. When there are n dislocations piled up at the GB under the resolved shear stress τ, a microcrack with length $2a$ will grow to release the local elastic energy. In this continuum model, the number of pile-up dislocations n can be calculated by the dislocation density multiplied by the pile-up length along the slip direction. It is worth mentioning that the size of microcrack is quite small compared with the crystal dimensions, and spontaneous growth of microcrack will not occur unless the material is under the action of applied stress. The crack length associated with dislocation pile-up can be written as Sarfarazi and Ghosh (1987)

$$2a=\frac{Gb^2(n_x^{GB})^2}{8\pi(1-\nu)\gamma_{eff}}=\lambda(n_x^{GB})^2, \tag{9}$$

where $\lambda\equiv Gb^2/[8\pi(1-\nu)\gamma_{eff}]$ is a constant related to the material properties, n_x^{GB} represents the number of pile-up dislocations at the GB with Burgers vector $\mathbf{b}$ projected in the x-direction. The pile-up dislocation density $n^{(i)}$ with Burgers vector $\mathbf{b}^{(i)}$ can be projected onto the x- and y-directions by $n_x^{(i)}b^{(i)}\equiv n^{(i)}\mathbf{b}^{(i)}\cdot\mathbf{e}_x=n^{(i)}\cos\theta^{(i)}b^{(i)}$ and $n_y^{(i)}b^{(i)}\equiv n^{(i)}\mathbf{b}^{(i)}\cdot\mathbf{e}_y=n^{(i)}\sin\theta^{(i)}b^{(i)}$, where $\theta^{(i)}$ is the angle between the slip direction $\mathbf{s}^{(i)}$ and the x-axis and $b^{(i)}$ is the magnitude of the Burgers vector $\mathbf{b}^{(i)}$. The x-component of the Burgers vector directly contributes to microcrack opening, while the y-component mediates GB sliding although it also influences microcrack propagation through its associated stress field. The x-component of the Burgers vector of all dislocations at the GB is $n_x^{GB}=n_x^{\alpha}+n_x^{\beta}$, representing that the pile-up dislocations from both sides of the GB can contribute to initiate a microcrack.

Substituting Eqs. (8) and (9) into Eq. (7), yields

$$M\equiv\left[(\sigma_{xx}^{GB})^2+(\sigma_{xy}^{GB})^2\right](n_x^{GB})^2=\frac{8G\gamma_{eff}}{\pi\lambda(1-\nu)}=\frac{64\gamma_{eff}^2}{b^2}, \tag{10}$$

where the last equality is obtained by substituting the expression for λ, yielding a more compact form. This equation is arranged such that the left-hand side only depends on the instantaneous state of the material while the right-hand side only depends on the intrinsic material properties. For simplicity, we define the left-hand side as $M\equiv\left[(\sigma_{xx}^{GB})^2+(\sigma_{xy}^{GB})^2\right](n_x^{GB})^2$ and treat the right-hand side as a constant $M^*\equiv 64\gamma_{eff}^2/b^2$ in the subsequent analysis. During our simulation, the stress components at the GB, σ_{xx}^{GB} and σ_{xy}^{GB}, and the number of local dislocations at the GB n_x^{GB} can be obtained at each step during the simulation process.

In summary, we propose a microcrack propagation criterion for our 2D model with infinite slip planes based on linear elastic fracture mechanics. The critical condition for crack propagation at the GB is given by Eq. (10), which relates the number of pile-up dislocations and the stress components σ_{xx}^{GB} and σ_{xy}^{GB} to the material properties. This criterion allows us to predict crack propagation in our model for the investigation of brittle fracture. It should be noted that we monitor both failure criteria, associated with necking and crack nucleation at the GB, during the simulations. Later, we will study which one dominates and determine which mechanism governs the failure of the material during the tensile test.

3. Results and discussions

Interfaces can affect both the plastic and fracture response of metallic alloys (Zhu and Wu, 2023; Huang et al., 2018; Zhu and Li, 2010). Herein, we examine the effects of interfaces on plastic deformation and fracture based on our proposed interface BC and continuum dislocation dynamics model under uniaxial tension in the x-direction; i.e., the model is loaded at a constant nominal strain rate $\dot{\epsilon}$. The model undergoes both elastic and plastic deformation. The plastic strain rate associated with slip system i can be calculated using the Orowan equation as $\dot{\gamma}^{(i)}=(\rho_+^{(i)}+\rho_-^{(i)})v_+^{(i)}b^{(i)}$, where $\rho_{+/-}^{(i)}$ and $v_{+/-}^{(i)}$, denote the density and velocity of positive/negative dislocations (Cai and Nix, 2016). The total plastic strain rate tensor can be obtained by summing over all slip systems and expressed as Cleveringa and Needleman (1997)

$$\dot{\boldsymbol{\epsilon}}^p=\sum_i\frac{\dot{\gamma}^{(i)}}{2}(\mathbf{s}^{(i)}\otimes\mathbf{n}^{(i)}+\mathbf{n}^{(i)}\otimes\mathbf{s}^{(i)}). \tag{11}$$

The stress rate is $\dot{\sigma}=E\dot{\epsilon}^e=E(\dot{\epsilon}-\dot{\epsilon}^p)$, where $\dot{\epsilon}$ is the nominal strain rate, $\dot{\epsilon}^p$ is the corresponding component of the plastic strain rate tensor $\dot{\boldsymbol{\epsilon}}^p$ along the loading direction, and E is the Young's modulus of the material (El-Awady et al., 2009; Zhang et al., 2021).

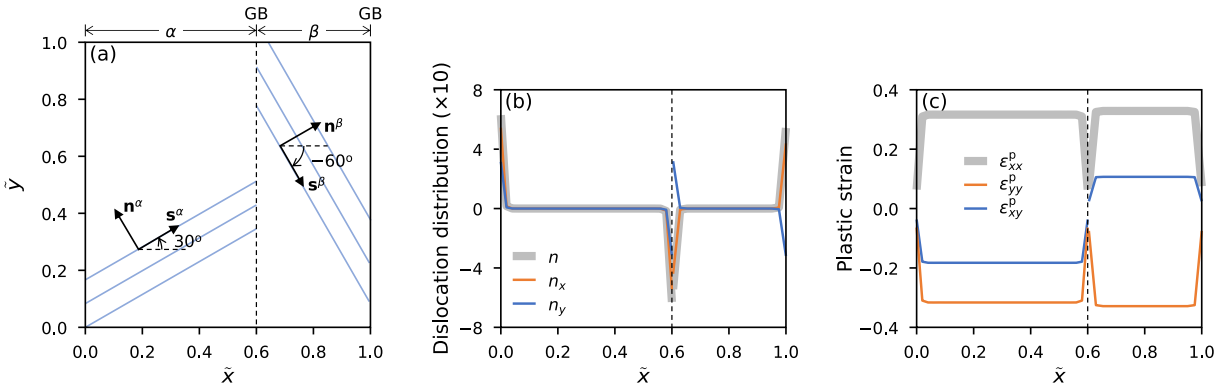

Fig. 5. (a) illustrates a schematic of the model, which consists of α and β grains, each containing only a single slip system. For the case with a reaction constant $\tilde{\kappa} = 10$, (b) presents the dislocation density distribution along the x-axis. The vertical black dashed lines indicate the positions of the grain boundaries (GBs). The gray, yellow, and blue lines correspond to the total dislocation density, and the dislocation density components projected along the x- and y-axes, respectively. (c) displays the spatial distribution of the three components of the plastic strain tensor. (For interpretation of the references to color in this figure legend, the reader is referred to the web version of this article.)

3.1. Effects of reaction constant on mechanical properties

We explore the influence of the reaction constant, $\tilde{\kappa}$, in a bicrystal system. The parameter $\tilde{\kappa}$ captures, in a coarse-grained manner, the effects of atomic-scale GB structure. For example, when a GB undergoes an interfacial phase transformation (Meiners et al., 2020), the $\tilde{\kappa}$ value should change. Although the explicit GB-structure dependence of $\tilde{\kappa}$ is not modeled here, this simplification allows us to explore the mesoscale consequences of GB-mediated mechanisms without unnecessary complexity. A natural extension of this interface reaction framework is to parameterize $\tilde{\kappa}$ by atomistic simulations. Incorporating such atomic-scale information would improve the model's predictive capability and link the mesoscale kinetics to the underlying atomic-scale mechanisms. Each grain contains only one slip system with misorientation angles of $\theta^\alpha = 30°$ and $\theta^\beta = -60°$, respectively. Therefore, the interface BC is a Robin boundary condition (reaction BC) with varying reaction constants, $\tilde{\kappa}$. The dislocation sources are assumed at each site, and an applied force is exerted along the x-axis, which is perpendicular to the interface, as shown in Fig. 5(a).

From Fig. 5(b), the distribution of dislocations along the x-axis is shown, as it is uniform in the y-direction. When an external force is applied to the model, dislocations with different signs move in opposite directions and are blocked by the GB denoted by the black dashed line in Fig. 5. The accumulation of dislocations at the GB induces back stress within the grain, resulting in strain hardening of the material. The number of dislocations $n^{(i)}$ is measured under the local coordinate system of each slip system. To measure the dislocation number in the global coordinate system, the x- and y-components of the dislocation number, n_x and n_y, are shown in Fig. 5(b). The corresponding plastic strains are plotted in Fig. 5(c).

In Fig. 6, the first two rows correspond to the results with reaction constants $\tilde{\kappa} = 10$ and 50, respectively. The stress–strain curves are plotted under different strain rates ($\tilde{\dot{\varepsilon}} = 5$ and 10), denoted by dashed and solid lines in Fig. 6(a1). These curves show that the strength increases with the applied strain rate. The onset strain of necking is shown in Fig. 6(a2) and (b2). The black and blue lines represent the strain hardening rate $\tilde{\Theta}$ (left-hand side of the Hart criterion) and $(1-m)\tilde{\sigma}$ (right-hand side of the Hart criterion) in Eq. (6), respectively. The intersection of these lines represents the onset point of necking. The necking process can be interpreted as follows: in the first stage, the strain hardening of the material grows more rapidly than stress localization, allowing the material to remain stable. As the external load continues to increase and exceeds the intersection point, the material starts to collapse because the rate of stress localization becomes larger than the strain hardening rate. Considering crack nucleation criterion, Fig. 6(a3) and (b3) depict the evolution of the value $\tilde{M} \equiv \left[(\tilde{\sigma}^{\mathrm{GB}}_{xx})^2 + (\tilde{\sigma}^{\mathrm{GB}}_{xy})^2\right](n^{\mathrm{GB}}_x)^2$ at the GB. The crack nucleates once the local value $\tilde{M}$ reaches a certain threshold value $\tilde{M}^*$ given by the right-hand side of Eq. (10). Here, the $\tilde{M}^*$ value is set to one, indicated by the orange horizontal line in Fig. 6(a3) or (b3), as an illustrative example. Once the ductile and brittle fracture strains are determined, the corresponding strength of the material can be read from the stress–strain curves, as shown by the orange lines in Fig. 6(a1) and (b1).

The dislocation fluxes represent the rate of dislocations reacted per unit length per unit time at the interface. The reaction constant $\tilde{\kappa}$, as shown in Eq. (3), controls the magnitude of the dislocation fluxes reacting at the interface. Therefore, it is crucial to explore the effect of the reaction constant $\tilde{\kappa}$ on the mechanical properties of the materials. Similar to the previous cases, stress–strain curves can be obtained for different reaction constants $\tilde{\kappa}$. Additionally, the onset strain of necking and crack nucleation can be determined by considering corresponding failure criteria.

On the one hand, there is a peak value $\tilde{\kappa}^*$ for the ductility of the material represented by the blue line with the increase of the reaction constant $\tilde{\kappa}$ as shown in Fig. 6(c). When the reaction constant $\tilde{\kappa}$ increases until it reaches $\tilde{\kappa}^*$, more dislocations can transmit across the GB, resulting in larger plastic deformation and increased ductility of the material. However, when $\tilde{\kappa}$ exceeds $\tilde{\kappa}^*$ and continues to increase, the reaction dislocation flux becomes too large, leading to minimal pile-up dislocations at the GB. As a result, the strain hardening term $\tilde{\Theta}$ in the Hart criterion Eq. (6) becomes significantly smaller, which in turn decreases the ductility of the material. It should be noted that our model does not consider any other strengthening mechanisms such as dislocation hardening, solid solution strengthening, precipitation hardening, and dispersion hardening, apart from the GB strengthening. In the extreme case where the reaction constant approaches infinity ($\tilde{\kappa} \to \infty$), the GB can hardly block any dislocations, resembling a single crystal. In such a case, no strain hardening occurs, and necking quickly initiates once an external stress is applied.

On the other hand, as the dislocations pile up against the GB, the increased local value $\tilde{M}$ at the GB, which is a function of pile-up dislocation number and local stress, may lead to crack nucleation at the GB according to the criterion Eq. (10). Once the local value $\tilde{M}$ exceeds a certain threshold value ($\tilde{M} \geq \tilde{M}^*$), the material undergoes brittle fracture at the GB, and the corresponding strain ε_{b} can be considered as the onset strain of crack nucleation, as shown in Fig. 6(a3). Comparing the two strains mentioned above, if $\varepsilon_{\mathrm{d}} < \varepsilon_{\mathrm{b}}$, the failure mode can be classified as ductile fracture; otherwise, it is brittle fracture ($\varepsilon_{\mathrm{d}} > \varepsilon_{\mathrm{b}}$). With an increase in the reaction constant $\tilde{\kappa}$, there is a transition point $\tilde{\kappa}_{\mathrm{T}}$ for the failure strain, as depicted in Fig. 6(c).

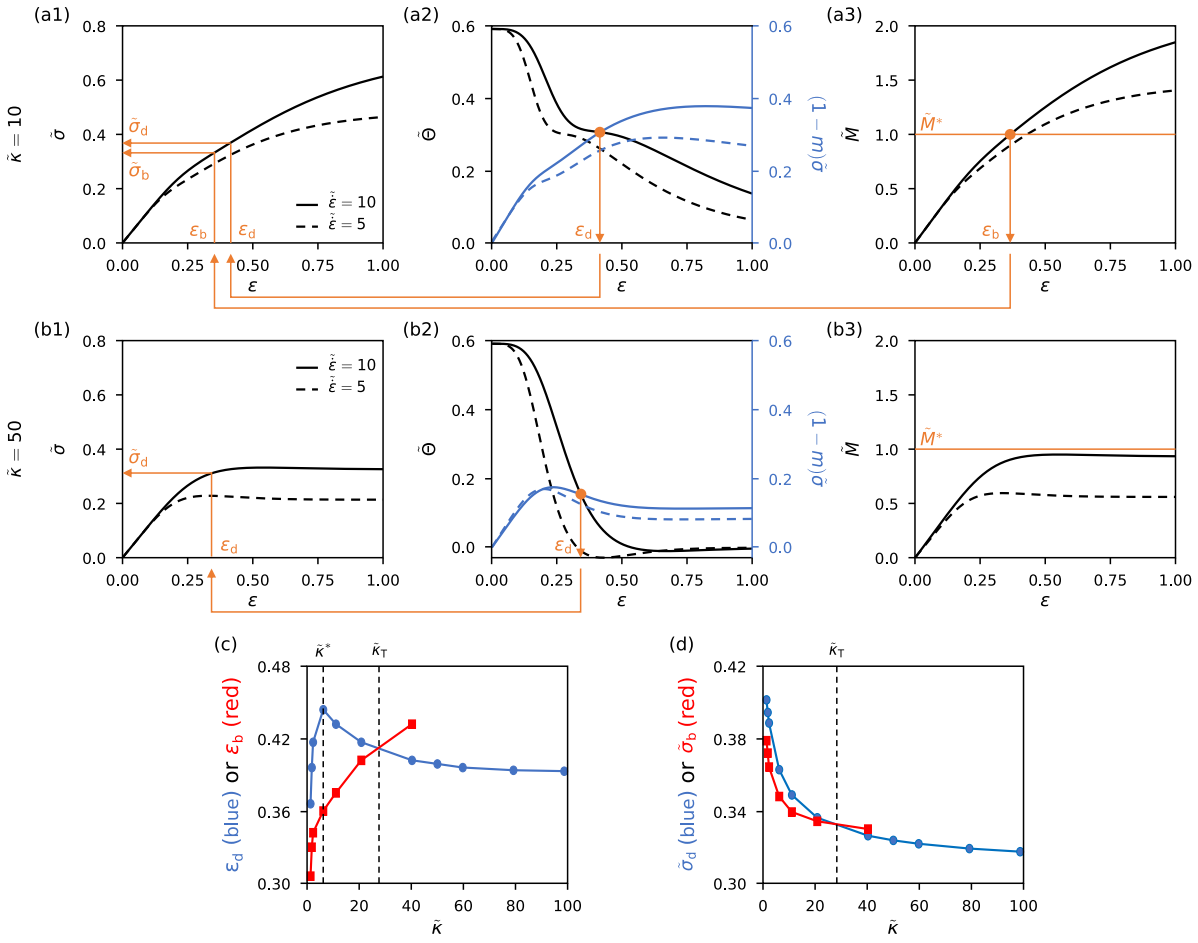

Fig. 6. Comparison of ductile and brittle fracture strains predicted by Hart and crack nucleation criteria, respectively. The first two row correspond to the results under the reaction constant $\tilde{\kappa} = 10$ and 50. (a1) and (b1) Stress–strain curve of material under different strain rate $\tilde{\dot{\varepsilon}}$ denoted by the solid and dashed lines respectively. (a2) and (b2) The black and blue lines represent strain hardening $\tilde{\Theta}$ and $(1-m)\tilde{\sigma}$ respectively. (a3) and (b3) Evolution of the local value $\tilde{M} \equiv \left[(\tilde{\sigma}^{\mathrm{GB}}_{xx})^2 + (\tilde{\sigma}^{\mathrm{GB}}_{xy})^2\right](n^{\mathrm{GB}}_x)^2$ near the GB under different strain rate and threshold value for interfacial strength denoted by orange horizontal line. (c) The ductile strain ε_d and brittle strain ε_b are plotted under different reaction constants $\tilde{\kappa}$. (d) The strength of the material corresponds to the brittle and ductile fracture under varying reaction constants. (For interpretation of the references to color in this figure legend, the reader is referred to the web version of this article.)

Below this transition point, the fracture mode is dominated by brittle fracture. When $\tilde{\kappa}$ gradually increases but remains below the transition point ($\tilde{\kappa} \le \tilde{\kappa}_T$), more pile-up dislocations can be transmitted to another grain, releasing the local tensile stress near the GB and resulting in an increase in the failure strain ε_b governed by brittle fracture. When the reaction constant $\tilde{\kappa}$ continues to increase and exceeds the point $\tilde{\kappa}_T$, the fracture mechanism transitions from brittle to ductile modes, causing a gradual decrease in the failure strain. It is worth mentioning that when $\tilde{\kappa}$ is sufficiently large, brittle fracture may vanish, as shown in Fig. 6(b3), since the local value $\tilde{M}$ at the GB induced by minimal pile-up dislocations never reach the critical value $\tilde{M}^*$.

From Fig. 6(d), the ultimate strength of the material also exhibits at the reaction constant $\tilde{\kappa}_T$. Initially, the strength is controlled by brittle fracture and then transitions to ductile fracture. As the reaction constant $\tilde{\kappa}$ increases, more dislocations react at the GB, resulting in fewer pile-up dislocations. The reduced number of pile-up dislocations leads to less strengthening of the material, causing the strength to decrease with an increase in the reaction constant $\tilde{\kappa}$, as shown in Fig. 6(d).

3.2. Transition of brittle and ductile fracture

Now we investigate the transition of ductile and brittle fracture by varying applied strain rates $\dot{\varepsilon}$ and reaction constants κ. Each grain has a single slip system, with $\theta^\alpha = 30°$ and $\theta^\beta = -60°$, respectively. A tensile stress was applied along the x-axis, and the corresponding loading rate was $\dot{\sigma} = E(\dot{\varepsilon} - \dot{\varepsilon}^{\mathrm{p}}_{xx})$. Other parameters are the same as in the previous cases (see Table 1). Under a fixed reaction constant κ, the materials exhibited a transition from ductile to brittle fracture as the applied strain rate increased. This indicates the existence of a transition strain rate corresponding to the shift in fracture behavior under a given reaction constant.

When the interfacial strength is set to 3.0 ($\tilde{M}^* = 3.0$), Fig. 7(a) illustrates the ductile fracture mode (represented by red dots) and brittle fracture mode (represented by blue squares) under different strain rates $\tilde{\dot{\varepsilon}}$ and reaction constants $\tilde{\kappa}$. The black solid line represents the boundary between ductile and brittle fracture based on the applied strain rate. It can be observed that a higher applied transition strain rate is required as the reaction constant $\tilde{\kappa}$ increases. Moreover, the required transition strain rate varies when considering materials with different interfacial strengths $\tilde{M}^*$. The transition strain rate line corresponding to different interfacial strengths $\tilde{M}^*$ can be obtained following the same method. Based on the three different transition lines, the transition surface can be interpolated as shown in Fig. 7(b). As depicted in Fig. 7(b), the corresponding transition strain rate increases with an increase in interfacial strength $\tilde{M}^*$.

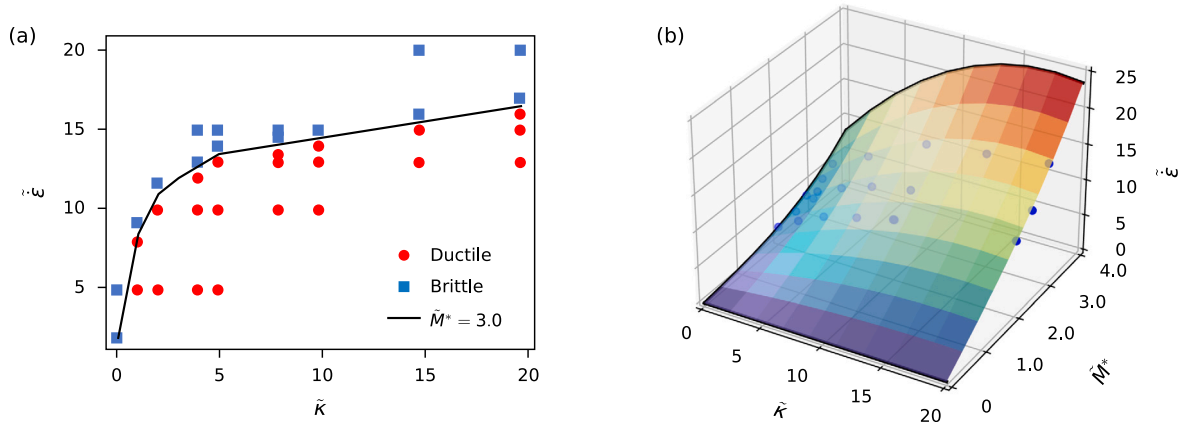

Fig. 7. (a) the black line denotes the transition strain rate line between ductile and brittle fracture when the interfacial strength is set to 3.0, where the red dot and blue squares represent the ductile and brittle fracture respectively; (b) the transition boundary between ductile and brittle fracture is denoted by the colored surface, where the blue dots represent the transition strain rate under different interfacial strength $\tilde{M}^*$ and reaction constant $\tilde{\kappa}$. (For interpretation of the references to color in this figure legend, the reader is referred to the web version of this article.)

3.3. Variation of strain hardening rate with strain

In our simulation, the strain hardening arises solely from the back stress induced by the accumulated dislocations at the interface. As a result, the strain hardening rate versus strain curve should exhibit significant variations under different reaction constants. Now we continue to investigate the strain hardening rate upturn by this 2D CDD model and the proposed interface BC. In these cases, each grain has one slip system, with $\theta^{\alpha} = 30°$ and $\theta^{\beta} = -60°$, respectively. The applied tensile force is along the x-axis, and the other parameters are the same as in the previous cases (see Table 1).

For a case with reaction constant of $\tilde{\kappa} = 2.0$ and dislocation source intensity $\tilde{\eta} = 10^9$, the strain hardening process can be classified into three stages as shown in Fig. 8(e). Initially, dislocations glide along the slip plane, causing plastic deformation of the material and leading to a decrease in $\tilde{\Theta}$. As dislocations pile up against the interface, the resulting back stress contributes to a transient increase in strain hardening. During this stage, the dislocation flux remains small, but dislocations accumulate rapidly. When a sufficient quantity of dislocations has piled up, the dislocation fluxes reacting at the interface increase significantly due to the penetrable/Robin interface boundary condition (Eq. (4)), leading to a decrease in the pile up and strain hardening rate. This whole process is illustrated schematically in Fig. 9(b1)–(b3). To elucidate it more clearly, the rate of pile-up dislocation at the interface is defined as $\tilde{\rho}(0)\Delta\tilde{x}\Delta\tilde{y}/\Delta\tilde{y} = \tilde{\rho}(0)\Delta\tilde{x}$, where $\Delta\tilde{x}$ and $\Delta\tilde{y}$ are the lengths of each mesh size. The corresponding dislocation flux $\tilde{J}^{\alpha}(0)$ and piled up rate $\tilde{\rho}^{\alpha}(0)\Delta\tilde{x}$ are also plotted for each case.

In the case of a larger reaction constant, $\tilde{\kappa} = 4.0$, dislocations can react quickly once they reach the interface as shown in Fig. 9(c1)–(c2). Consequently, only a small number of dislocations pile up, resulting in limited back stress and a slower increase in strain hardening. The strain hardening rate during the loading process does not exhibit a pronounced Θ-upturn, as shown in Fig. 8(h). In the extreme case where the interface BC is impenetrable ($\tilde{\kappa} = 0$), all dislocations are blocked from piling up against the interface as schematically shown in Fig. 9(a1)–(a2). This leads to an initial decrease and subsequent constant strain hardening rate throughout the loading process, as depicted in Fig. 8(b). In this scenario, the theoretical ductility is quite strong, as evidenced by the constant strain hardening rate denoted by the solid black line in Fig. 8(b). It should be noted that in experiments, typically only the decrease in strain hardening can be observed, as materials often undergo brittle fracture before reaching the stage of constant strain hardening. Hence, there is a competition between the rate of dislocation pile-up progress and the dislocation reaction rate at the interface, as shown in Fig. 9(b1)–(b3) and (c1)–(c2). When the source intensity $\tilde{\eta}$ increases while keeping the reaction constant the same, the phenomenon of Θ-upturn gradually becomes more pronounced due to the dominance of the dislocation accumulation rate in these cases as shown in Fig. 8(d)–(f) or (g)–(i). On the contrary, the Θ-upturn gradually vanishes, and even the stress softening of the materials occurs when the source intensity $\tilde{\eta} = 10^8$ as Fig. 8(d) and (g) show.

The experimental observations, such as those in Fig. 1, can be understood based on the above analysis. In coarse-grained (CG) samples, GBs play a negligible role. Dislocation generation is dominated by intragranular sources (like Frank–Read sources), and hardening arises primarily from dislocation–dislocation interactions, which typically do not produce a Θ-upturn. In nanocrystalline or ultrafine-grained (UFG) samples, intragranular sources are scarce; GBs provide the primary dislocation sources (Van Swygenhoven and Weertman, 2006; Gautier et al., 2025). GBs act both as dislocation sources and barriers to dislocation motion. Both source and barrier mechanisms are governed by interface reactions with comparable reaction constants. When dislocation generation rates balance dislocation transmission rates at GBs, strain hardening rate remains low and no Θ-upturn occurs. In UFG/CG sandwich structures, particularly near the interfaces between UFG and CG domains, GBs are available as effective dislocation barriers while robust intragranular sources operate concurrently. Under this condition, the mechanism depicted in Fig. 9(b1)–(b3) works and Θ-upturn is expected, corresponding to the bottom-right cases Fig. 8.

As shown in Fig. 10, with the reaction constant $\tilde{\kappa}$ increasing, the Θ-upturn gradually weakens and eventually disappears. At sufficiently large $\tilde{\kappa}$, the material may even exhibit softening, i.e., $\tilde{\Theta} < 0$. The intersection of $\tilde{\Theta}$ (solid curves) with $(1-m)\tilde{\sigma}$ (dashed curves) marks the onset of ductile fracture following necking, according to Eq. (6). The presence of Θ-upturn significantly delays necking. These results suggest that maintaining good ductility requires an intermediate $\tilde{\kappa}$: if $\tilde{\kappa}$ is too large, strain hardening is suppressed and necking is promoted; if $\tilde{\kappa}$ is too small, as in the limit of impenetrable GBs, rapid Burgers vector accumulation leads to brittle intergranular fracture.

The limitations in our simulations are briefly discussed below. First, we have assumed that there is a single slip system in each grain in all cases. Our interface model can be applied to the cases of multiple slip systems (see our previous work (Yu et al., 2024)). But, we intentionally simplify the intragranular plasticity here to isolate GB effects under controlled conditions. Including multiple slip systems would introduce substantial work hardening via dislocation–dislocation interactions within grains, thus hiding the GB effects. Second, although the present analysis is restricted to 2D, we expect some of the interface-mediated trends identified here may remain qualitatively relevant in 3D systems; however, this requires further investigation. Nevertheless, we choose the 2D numerical examples to

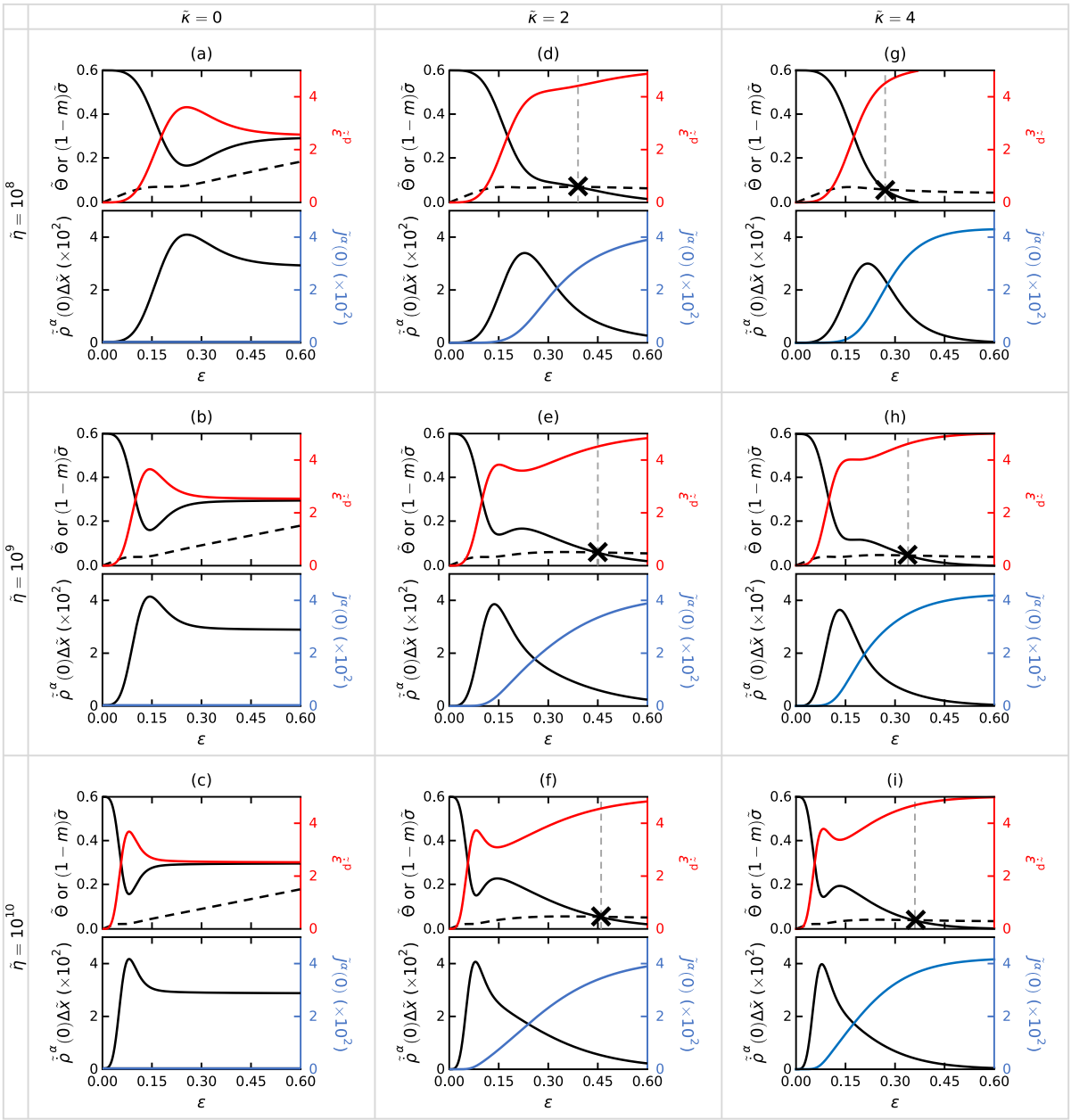

Fig. 8. Evolution of key physical quantities with strain for various interface reaction constants $\tilde{\kappa}$ and intragranular source intensity η. For each $(\tilde{\kappa}, \tilde{\eta})$ case, the upper panel shows the strain hardening rate $\tilde{\Theta}$ (black solid curve), the quantity $(1-m)\tilde{\sigma}$ (*c.f.* Eq. (6); black dashed curve), and plastic strain rate $\dot{\tilde{\varepsilon}}^{\mathrm{p}}$ (red curve). The lower panel shows the rate of dislocation pile-up $\dot{\tilde{\rho}}^{\alpha}(0)\Delta\tilde{x}$ (black curve) and dislocation flux $\tilde{J}^{\alpha}(0)$ (blue curve) at the GB on the side of grain α. Crosses "×" denote the onsets of necking. (For interpretation of the references to color in this figure legend, the reader is referred to the web version of this article.)

simplify the description of intragranular plasticity, reduce the parameter space, and focus on the GB-mediated behavior. The present model is most applicable to polycrystalline materials with intermediate grain sizes, where both intragranular dislocation activity and dislocation-GB interactions are important. Its applicability becomes limited for coarse-grained materials with a very low GB density and for nanocrystalline materials with extremely small grain sizes (e.g., below 40 nm), where conventional lattice-dislocation plasticity is largely suppressed and GB-mediated deformation mechanisms dominate.

4. Conclusions

In this work, we elucidated the role of grain boundaries in mediating the macroscopic mechanical behavior of polycrystalline materials. Based on mesoscale simulations and analysis, our findings are summarized as below:

(i) For a fixed applied strain rate $\dot{\varepsilon}$ and interfacial strength M^*, increasing the interfacial Burgers-vector reaction constant κ shifts the failure mode from brittle to ductile fracture. Therefore, there exists a value κ_{T} marking this brittle-to-ductile transition. Additionally, there exists another critical reaction constant κ^* corresponding to maximum ductility. Below κ^*, ductility improves with increase of κ as more dislocations can react at the interface and promote plasticity. Beyond κ^*, ductility decreases with increase of κ due to diminished strain hardening. Note that this study only considers strengthening mechanisms arising from dislocation-grain boundary interactions, excluding other contributions such as Taylor hardening or precipitation hardening.

(ii) For a particular reaction constant κ, increasing the applied strain rate $\dot{\varepsilon}$ can switch the failure mode from ductile to brittle fracture. A transition strain rate exists that delimits the regimes of ductile and brittle fracture for a given reaction constant. The trend shows

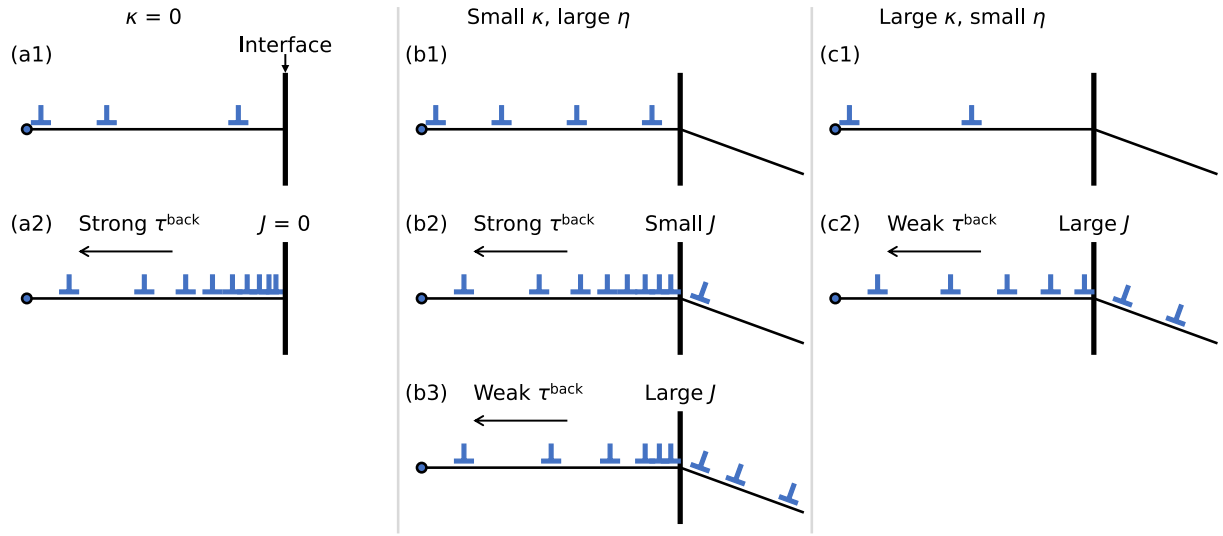

Fig. 9. (a1)–(a2), (b1)–(b3), and (c1)–(c2) show the processes of dislocation accumulation and transmission near the interface with the increase of reaction constant κ.

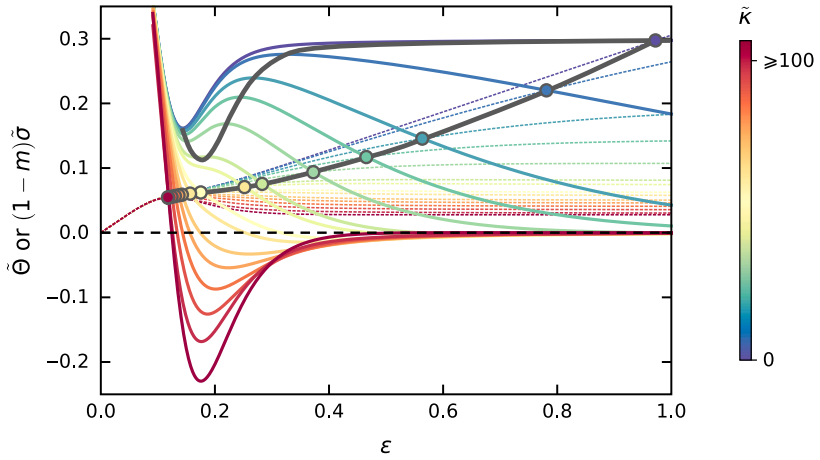

Fig. 10. Strain hardening rate $\tilde{\Theta}$ (solid curves) and $(1-m)\tilde{\sigma}$ (dotted curves) are plotted under different reaction constants ($\tilde{\kappa}$). Instability points are indicated by circles.

that a higher transition strain rate is required as the reaction constant increases; and for a material with weaker interfacial strength M^*, a lower transition strain rate is required.

(iii) The observed variation in strain hardening rate with strain can be rationalized by the competition between the rate of dislocation pileup and the dislocation reaction rate at grain boundaries. Initially, strain hardening rate decreases as dislocation sources are activated and dislocation glide occurs within grains. As dislocation pile-ups form and back stresses develop, strain hardening rate transiently increases. With further deformation, dislocation reactions proceed, the effect of pile-up weakens, and strain hardening rate declines again. For the case where κ is large, dislocation reactions dominate, resulting in weak strain hardening. So, the strain hardening upturn diminishes with increasing reaction constant, while it can be enhanced by improving dislocation generation rates.

In conclusion, failure modes in polycrystalline materials are partially governed by the kinetics of Burgers-vector reactions at interfaces. The proposed framework provides an approach to incorporate interfacial properties into predictive models of mechanical behaviors, offering insights for grain-boundary engineering and microstructural design.

CRediT authorship contribution statement

Jinxin Yu: Writing – review & editing, Writing – original draft, Visualization, Validation, Software, Investigation, Formal analysis, Conceptualization. **Alfonso H.W. Ngan:** Writing – review & editing, Supervision, Conceptualization. **David J. Srolovitz:** Writing – review & editing, Supervision, Investigation, Funding acquisition, Formal analysis, Conceptualization. **Jian Han:** Writing – review & editing, Supervision, Investigation, Conceptualization.

Declaration of competing interest

The authors declare the following financial interests/personal relationships which may be considered as potential competing interests: Jinxin Yu Jian Han David J. Srolovitz Alfonso Hing Wan Ngan

Acknowledgments

JH and DJS were supported by the Hong Kong Research Grants Council Collaborative Research Fund C7140-25GF. JH also acknowledges support of the Hong Kong Research Grants Council General Research Fund CityU 11213425. AHWN acknowledges support from the

Shenzhen Fund 2021 Basic Research General Programme JCY20210324115400002 and the Guangdong Province Basic and Applied Research Key Project 2020B0301030001.

Appendix A. Numerical simulation

Consider a unit cell which is bounded at $x = 0$ and L_x along the $\mathbf{e}_x$-axis and bounded at $y = 0$ and L_y along the $\mathbf{e}_y$-axis as shown in Fig. 2. Discretize the x and y coordinate by $x_i = i\Delta x$ $(i = 0, \ldots, N_x)$ and $y_j = j\Delta y$ $(j = 0, \ldots, N_y)$ respectively, where the interval is $\Delta x = L_x/N_x$ and $\Delta y = L_y/N_y$. Discretize the time t by $t_n = n\Delta t$ $(n = 0, 1, \ldots)$, where Δt is the time step.

Step 0 Calculate the initial resolved shear stress and set the initial dislocation density

$$\tau^{(i)}(x_i, y_j, 0) = \sigma_{xx}(x_i, y_j, 0)s_x^{(i)}n_x^{(i)} + \sigma_{yy}(x_i, y_j, 0)s_y^{(i)}n_y^{(i)} + \sigma_{xy}(x_i, y_j, 0)(s_x^i n_y^{(i)} + s_y^{(i)}n_x^{(i)}), \tag{A.1}$$

$$\rho_+^{(i)}(x_i, y_j, 0) = \rho_-^{(i)}(x_i, y_j, 0) = \rho_0^{(i)}, \tag{A.2}$$

where $\mathbf{s}^{(i)}$ and $\mathbf{n}^{(i)}$ are the slip direction and unit normal direction of i slip plane respectively.

Step 1 Calculate the velocity at each site by

$$v_+^{(i)}(x_i, y_j, t_n) = v_0\left(\frac{\tau^{(i)}(x_i, y_j, t_n) - \tau_f}{\tau_0}\right)^n,$$
$$v_-^{(i)}(x_i, y_j, t_n) = -v_+^{(i)}(x_i, y_j, t_n) \quad (i, j = 0, \ldots, N). \tag{A.3}$$

Step 2 Apply one of the BCs:
Dirichlet BC: let $\rho_{+/-}^{(i)}(x_0, t_n) = \rho_{+/-}^{(i)}(x_N, t_n) = 0$;
Neumann BC: let $\rho_{+/-}^{(i)}(x_0, t_n)v_{+/-}^{(i)}(x_0, t_n) = \rho_{+/-}^{(i)}(x_N, t_n)v_{+/-}^{(i)}(x_N, t_n) = 0$;
Robin BC: let $\rho_{+/-}^{(i)}(x_0, t_n)v_{+/-}^{(i)}(x_0, t_n) = \rho_{+/-}^{(i)}(x_N, t_n)v_{+/-}^{(i)}(x_N, t_n) = \boldsymbol{J}_{+/-}^{(i)}$.

Step 3 Integrate the differential equations by the finite difference method. First, the net source which is the sum of the generation term and the annihilation terms can be expressed as

$$\dot{\rho}^{(i),\text{source}}(x_i, y_j, t_n) = -r_c\rho_+^{(i)}(x_i, y_j, t_n)\rho_-^{(i)}(x_i, y_j, t_n)\left|v_+^{(i)}(x_i, y_j, t_n) - v_-^{(i)}(x_i, y_j, t_n)\right| + \eta|\tau^{(i)}(x_i, y_j, t_n)|^p. \tag{A.4}$$

The new positive/negative dislocation densities at each site are updated by the evolution equations Eq. (1). In order to handle high gradients, a total variation diminishing scheme must be introduced, usually Monotone Upstream-centered Schemes for Conservation laws (MUSCL) are employed. Here, we used the Kurganov–Tadmor central scheme, which is a second-order, high-resolution MUSCL construction. Since it is applicable to all slip systems within each grain, for the sake of brevity, the slip system denoted by subscript "(i)" and subscript "$+/-$" sign for positive/negative dislocations are omitted here. With this, the flux operator above is re-cast into the semi-discrete form (Wesseling, 2009):

$$\frac{d\rho_i}{dt} + \frac{1}{\Delta x_i}[(\rho v)_{i+1/2} - (\rho v)_{i-1/2}] + \cdots \tag{A.5}$$

where:

$$\rho_i \equiv \rho(x_i, t_n); \quad (\rho v)_{i\pm1/2} = \frac{1}{2}[\rho_{i\pm1/2}^R v_{i\pm1/2} - \rho_{i\pm1/2}^L v_{i\pm1/2}] - \max[|v_i|, |v_{i\pm1}|][\rho^R - \rho^L]; \tag{A.6}$$

$$\rho_{i+1/2}^L = \rho_i + 0.5\Phi(r_i)(\rho_{i+1} - \rho_i); \quad \rho_{i+1/2}^R = \rho_i - 0.5\Phi(r_{i+1})(\rho_{i+2} - \rho_{i+1}); \tag{A.7}$$

$$\rho_{i-1/2}^L = \rho_{i-1} + 0.5\Phi(r_{i-1})(\rho_i - \rho_{i-1}); \quad \rho_{i-1/2}^R = \rho_i - 0.5\Phi(r_i)(\rho_{i+1} - \rho_i); \tag{A.8}$$

$$r_i = \frac{\rho_i - \rho_{i-1}}{\rho_{i+1} - \rho_i}; \quad \Phi(r) = \frac{2r}{1 + r^2}; \tag{A.9}$$

Here, $\Phi(r)$ is the flux limiter, which is a function such that for $r < 0$, $\Phi = 0$ and $\Phi = 1$ for $r = 1$. The main idea of MUCSL is to use slope limited left and right extrapolated states for the cell's approximation, and the left and right states are those at the cell walls, i.e., $i = \pm1/2$. Also MUSCL is combined with the Runge–Kutta time marching method to obtain accurate results.

Step 4 Calculate the net dislocation density:

$$\rho^{(i)}(x_i, y_i, t_n) = \rho_+^{(i)}(x_i, y_i, t_n) - \rho_-^{(i)}(x_i, y_i, t_n), \tag{A.10}$$

The dissociation of dislocation densities with respect to Burgers vector b_x and b_y are

$$\rho^{\dashv}(x_i, y_i, t_n) = \sum_i \rho^{(i)}(x_i, y_i, t_n)\cos\theta^{(i)}, \quad \rho^{\perp}(x_i, y_i, t_n) = \sum_i \rho^{(i)}(x_i, y_i, t_n)\sin\theta^{(i)}. \tag{A.11}$$

Step 5 Update the stress field of the model

$$\sigma_{kl}(x_i, y_j, t_{n+1}) = \sigma_{kl}^{\text{ext}}(x_i, y_j, t_n) + \sum_{i'=0}^{N_x}\sum_{j'=0}^{N_y}\rho^{\dashv}(x_{i'}, y_{j'}, t_n)\sigma_{kl}^{\text{w}\dashv}((i' - i)\Delta x, (j' - j)\Delta y)\Delta x\Delta y + \tag{A.12}$$

$$\sum_{i'=0}^{N_x}\sum_{j'=0}^{N_y}\rho^{\perp}(x_{i'}, y_{j'}, t_n)\sigma_{kl}^{\text{w}\perp}((i' - i)\Delta x, (j' - j)\Delta y)\Delta x\Delta y, \tag{A.13}$$

where σ_{kl} represents σ_{xy}, σ_{xx}, and σ_{yy}, $\sigma_{kl}^{\text{w}\dashv}$ and $\sigma_{kl}^{\text{w}\perp}$ are the corresponding stress kernels as supplementary material shows.

Step 6 Update the resolved shear stress by Eq. (A.1), then go to **Step 1**.

Appendix B. Supplementary data

Supplementary material related to this article can be found online at https://doi.org/10.1016/j.mechmat.2026.105798.

Data availability

Data will be made available on request.

References

Argon, A.S., 2007. Strengthening Mechanisms in Crystal Plasticity. Oxford University Press.

Cai, W., Nix, W.D., 2016. Imperfections in Crystalline Solids. Cambridge University Press.

Cleveringa, H., Needleman, A., 1997. Comparison of discrete dislocation and continuum plasticity predictions for a composite material. Acta Mater. 45 (8), 3163–3179. http://dx.doi.org/10.1016/S1359-6454(97)00011-6.

Cottrell, A.H., 1965. Mechanics of fracture in large structures. Proc. R. Soc. Lond. Ser. A. Math. Phys. Sci. 285 (1400), 10–21. http://dx.doi.org/10.1098/rspa.1965.0085.

El-Awady, J.A., Wen, M., Ghoniem, N.M., 2009. The role of the weakest-link mechanism in controlling the plasticity of micropillars. J. Mech. Phys. Solids 57 (1), 32–50. http://dx.doi.org/10.1016/j.jmps.2008.10.004.

Gautier, R., Mompiou, F., Renk, O., Coupeau, C., Combe, N., Seine, G., Legros, M., 2025. Quantifying grain boundary deformation mechanisms in small-grained metals. Nature 648 (8093), 327–332. http://dx.doi.org/10.1038/s41586-025-09800-7.

Hall, E., 1951. The deformation and ageing of mild steel: III discussion of results. Proc. Phys. Soc. Sect. B 64 (9), 747. http://dx.doi.org/10.1088/0370-1301/64/9/303.

Hart, E., 1967. Theory of the tensile test. Acta Metall. 15 (2), 351–355. http://dx.doi.org/10.1016/0001-6160(67)90211-8.

Hirth, J.P., Lothe, J., 1982. Theory of Dislocations. John Wiley & Sons.

Huang, C., Wang, Y., Ma, X., Yin, S., Höppel, H., Göken, M., Wu, X., Gao, H., Zhu, Y., 2018. Interface affected zone for optimal strength and ductility in heterogeneous laminate. Mater. Today 21 (7), 713–719. http://dx.doi.org/10.1016/j.mattod.2018.03.006.

Javaid, F., Pouriayevali, H., Durst, K., 2021. Dislocation-grain boundary interactions: Recent advances on the underlying mechanisms studied via nanoindentation testing. J. Mater. Res. 36 (12), 2545–2557. http://dx.doi.org/10.1557/s43578-020-00096-z.

Ji, W., Zhou, R., Viveganantha, P., Wu, M.S., Gao, H., Zhou, K., 2023. Recent progress in gradient-structured metals and alloys. Prog. Mater. Sci. 101194. http://dx.doi.org/10.1016/j.pmatsci.2023.101194.

Jiang, M., Devincre, B., Monnet, G., 2019. Effects of the grain size and shape on the flow stress: A dislocation dynamics study. Int. J. Plast. 113, 111–124. http://dx.doi.org/10.1016/j.ijplas.2018.09.008.

Kacher, J., Eftink, B., Cui, B., Robertson, I., 2014. Dislocation interactions with grain boundaries. Curr. Opin. Solid State Mater. Sci. 18 (4), 227–243. http://dx.doi.org/10.1016/j.cossms.2014.05.004.

Kacher, J., Robertson, I., 2012. Quasi-four-dimensional analysis of dislocation interactions with grain boundaries in 304 stainless steel. Acta Mater. 60 (19), 6657–6672. http://dx.doi.org/10.1016/j.actamat.2012.08.036.

Kacher, J., Robertson, I.M., 2014. In situ and tomographic analysis of dislocation/grain boundary interactions in α-titanium. Phil. Mag. 94 (8), 814–829. http://dx.doi.org/10.1080/14786435.2013.868942.

Kheradmand, N., Barnoush, A., Vehoff, H., 2010. Investigation of the role of grain boundary on the mechanical properties of metals. In: Journal of Physics: Conference Series, vol. 240, IOP Publishing, 012017. http://dx.doi.org/10.1088/1742-6596/240/1/012017.

Kocks, U.F., Argon, A.S., Ashby, M.F., 1975. Kinetics. In: Thermodynamics and Kinetics of Slip, vol. 19, pp. 68–109.

Leung, H.S., Leung, P.S.S., Cheng, B., Ngan, A.H.W., 2015. A new dislocation-density-function dynamics scheme for computational crystal plasticity by explicit consideration of dislocation elastic interactions. Int. J. Plast. 67, 1–25. http://dx.doi.org/10.1016/j.ijplas.2014.09.009.

Li, X., Wei, Y., Lu, L., Lu, K., Gao, H., 2010. Dislocation nucleation governed softening and maximum strength in nano-twinned metals. Nature 464 (7290), 877–880. http://dx.doi.org/10.1038/nature08929.

Liu, W., Cheng, Y., Sui, H., Fu, J., Duan, H., 2023. Microstructure-based intergranular fatigue crack nucleation model: Dislocation transmission versus grain boundary cracking. J. Mech. Phys. Solids 173, 105233. http://dx.doi.org/10.1016/j.jmps.2023.105233.

Lu, L., Shen, Y., Chen, X., Qian, L., Lu, K., 2004. Ultrahigh strength and high electrical conductivity in copper. Science 304 (5669), 422–426. http://dx.doi.org/10.1126/science.1092905.

Meiners, T., Frolov, T., Rudd, R.E., Dehm, G., Liebscher, C.H., 2020. Observations of grain-boundary phase transformations in an elemental metal. Nature 579 (7799), 375–378. http://dx.doi.org/10.1038/s41586-020-2082-6.

Meyers, M.A., Mishra, A., Benson, D.J., 2006. Mechanical properties of nanocrystalline materials. Prog. Mater. Sci. 51 (4), 427–556. http://dx.doi.org/10.1016/j.pmatsci.2005.08.003.

Ngan, A.H.W., 2017. Dislocation-density kinematics: a simple evolution equation for dislocation density involving movement and tilting of dislocations. MRS Commun. 7 (3), 583. http://dx.doi.org/10.1557/mrc.2017.66.

Ovid'Ko, I., Valiev, R., Zhu, Y., 2018. Review on superior strength and enhanced ductility of metallic nanomaterials. Prog. Mater. Sci. 94, 462–540. http://dx.doi.org/10.1016/j.pmatsci.2018.02.002.

Sarfarazi, M., Ghosh, S., 1987. Microfracture in polycrystalline solids. Eng. Fract. Mech. 27 (3), 257–267. http://dx.doi.org/10.1016/0013-7944(87)90144-5.

Scardia, L., Peerlings, R.H., Peletier, M.A., Geers, M.G., 2014. Mechanics of dislocation pile-ups: a unification of scaling regimes. J. Mech. Phys. Solids 70, 42–61. http://dx.doi.org/10.1016/j.jmps.2014.04.014.

Smith, E., Barnby, J., 1967. Crack nucleation in crystalline solids. Met. Sci. J. 1 (1), 56–64. http://dx.doi.org/10.1179/msc.1967.1.1.56.

Stroh, A.N., 1957. A theory of the fracture of metals. Adv. Phys. 6 (24), 418–465. http://dx.doi.org/10.1080/00018735700101406.

Van Swygenhoven, H., Weertman, J.R., 2006. Deformation in nanocrystalline metals. Mater. Today 9 (5), 24–31. http://dx.doi.org/10.1016/S1369-7021(06)71494-8.

Wang, Y., Huang, C., Ma, X., Zhao, J., Guo, F., Fang, X., Zhu, Y., Wei, Y., 2023. The optimum grain size for strength-ductility combination in metals. Int. J. Plast. 164, 103574. http://dx.doi.org/10.1016/j.ijplas.2023.103574.

Weertman, J., 1996. Dislocation Based Fracture Mechanics. World Scientific.

Wesseling, P., 2009. Principles of Computational Fluid Dynamics, vol. 29, Springer Science & Business Media.

Wu, X., Jiang, P., Chen, L., Yuan, F., Zhu, Y.T., 2014. Extraordinary strain hardening by gradient structure. Proc. Natl. Acad. Sci. 111 (20), 7197–7201. http://dx.doi.org/10.1073/pnas.1324069111.

Wu, X., Yang, M., Yuan, F., Wu, G., Wei, Y., Huang, X., Zhu, Y., 2015. Heterogeneous lamella structure unites ultrafine-grain strength with coarse-grain ductility. Proc. Natl. Acad. Sci. 112 (47), 14501–14505. http://dx.doi.org/10.1073/pnas.1517193112.

Yang, M., Yuan, F., Xie, Q., Wang, Y., Ma, E., Wu, X., 2021. Strain hardening in Fe-16Mn-10Al-0.86 C-5Ni high specific strength steel. In: Heterostructured Materials. Jenny Stanford Publishing, pp. 721–747. http://dx.doi.org/10.1016/j.actamat.2016.02.044.

Yu, J., Ngan, A.H., Srolovitz, D.J., Han, J., 2024. Application of rigorous interface boundary conditions in mesoscale plasticity simulations. Modelling Simul. Mater. Sci. Eng. 32 (3), 035020. http://dx.doi.org/10.1088/1361-651X/ad26a0.

Yu, J., Ngan, A.H., Srolovitz, D.J., Han, J., 2025. Mesoscale description of interface-mediated plasticity. Acta Mater. 283, 120552. http://dx.doi.org/10.1016/j.actamat.2024.120552.

Zhang, X., Lu, S., Zhang, B., Tian, X., Kan, Q., Kang, G., 2021. Dislocation-grain boundary interaction-based discrete dislocation dynamics modeling and its application to bicrystals with different misorientations. Acta Mater. 202, 88–98. http://dx.doi.org/10.1016/j.actamat.2020.10.052.

Zhu, Y., Ameyama, K., Anderson, P.M., Beyerlein, I.J., Gao, H., Kim, H.S., Lavernia, E., Mathaudhu, S., Mughrabi, H., Ritchie, R.O., et al., 2021. Heterostructured materials: superior properties from hetero-zone interaction. Mater. Res. Lett. 9 (1), 1–31. http://dx.doi.org/10.1080/21663831.2020.1796836.

Zhu, T., Li, J., 2010. Ultra-strength materials. Prog. Mater. Sci. 55 (7), 710–757. http://dx.doi.org/10.1016/j.pmatsci.2010.04.001.

Zhu, T., Li, J., Samanta, A., Kim, H.G., Suresh, S., 2007. Interfacial plasticity governs strain rate sensitivity and ductility in nanostructured metals. Proc. Natl. Acad. Sci. 104 (9), 3031–3036. http://dx.doi.org/10.1073/pnas.0611097104.

Zhu, Y., Wu, X., 2023. Heterostructured materials. Prog. Mater. Sci. 131, 101019. http://dx.doi.org/10.1016/j.pmatsci.2022.101019.